Fate and Transport of Pharmaceuticals in Iron and Manganese Binary Oxide Coated Sand Columns

Tao Luo, Rasesh Pokharel, Tao Chen, Jean-François Boily, Khalil Hanna

Fate and Transport of Pharmaceuticals in Iron and Manganese Binary Oxide Coated Sand Columns

Tao Luo[a,c,†], Rasesh Pokharel[b,†], Tao Chen[a], Jean-François Boily[c], Khalil Hanna [a,d,*]

[a] Univ Rennes, Ecole Nationale Supérieure de Chimie de Rennes, CNRS, ISCR-UMR 6226, F-35000, Rennes, France.

[b] Department of Earth Sciences, Utrecht University, 3584 CB Utrecht, Netherlands

[c] Department of Chemistry, Umeå University, Umeå, SE-901 87, Sweden

[d] Institut Universitaire de France (IUF), MESRI, 1 rue Descartes, 75231 Paris, France.

*Corresponding author: Tel.: +33 2 23 23 80 27, khalil.hanna@ensc-rennes.fr

25 **Graphical Abstract**

26

27

28

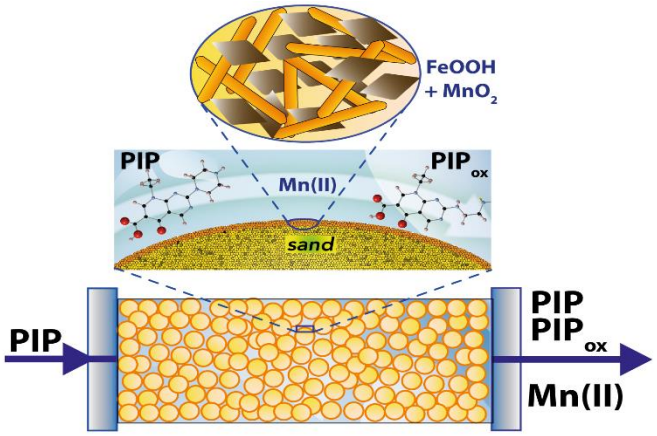

Abstract

Predicting the fate and transport of pharmaceuticals in terrestrial environments requires knowledge of their interactions with complex mineral assemblages. To advance knowledge along this front, we examined the reactivity of pipemidic acid (PIP), a typical quinolone antibiotic, with quartz particles coated with a mixture of manganese oxide (MnO_2) and goethite (α-FeOOH) under static and dynamic flow conditions. Batch and dynamic column experiments showed that PIP binding to MnO_2 proceeded through a heterogeneous redox reaction while binding to goethite was not redox-reactive. Mixed columns of aggregated goethite-manganese particles however enhanced redox reactivity because (i) goethite facilitated the transport of dissolved Mn(II) ion and increased the retention of PIP oxidation products, and (ii) MnO_2 was protected from passivation. This mobility behavior was predicted using transport models accounting for adsorption and transformation kinetics of PIP on both goethite and MnO_2. This work sheds new light on reactivity changes of mixtures of Fe and Mn oxides under flow-through conditions, and will have important implications in predicting the fate and transport of redox-active organic compounds as well as development of new geomedia filters for environmental remediation.

Keywords: pharmaceuticals; goethite; manganese oxide; redox; geomedia filter; transport; modeling.

Synopsis

This work shows how goethite may overcome the drawbacks of Mn-oxides to be used as a geomedia-filter for environmental remediation

Introduction

Iron (Fe) and manganese (Mn) are the two most common redox-active elements in the Earth's crust. They are present in wide range of environments with different composition, mineralogy, and morphology[1,2]. For example, Fe and Mn-oxides may co-exist with each other as discrete particles, mixture of component phases or particulate coatings in soils and sediments[3]. In deep sea waters, Mn and Fe are oxidized to form ferromanganese crusts and nodules on the oceans floor, a mineral of immense economic interest. Because of their specific nanoscale properties, high surface area, low cost, strong oxidation and sorption abilities, iron and manganese oxides are widely used in various environmental applications [4–8]. They play a key role in controlling the fate and mobility of elements and toxic compounds in nature, and can also be used as an environmentally friendly geomedia filter in water treatment technologies and/or aquifer recharge management [9–11].

Goethite (α-FeOOH) is one of the most thermodynamically stable iron oxyhydroxide under ambient conditions, and the most abundant one in natural settings[2,12]. For this reason, numerous theoretical and experimental studies explored organic or inorganic compounds binding mechanisms to goethite surfaces and their impact on migration in nature[13,14]. Birnessite-type layered manganese oxides are, at the same time, of great interest given their strong redox- and cation exchange reactivity[8,15,16]. Their interest is also motivated by their structural similarity to the biogenically precipitated natural manganese oxides, which are the most commonly occurring forms of MnO_2 in surficial environments[1].

Although the reactivity of each individual or single phase has been widely investigated [7,17–21], knowledge is limited on how binary mixture of these two phases, goethite and MnO_2, alter the overall reactivity of environmental compounds. Previous studies[22–24] have reported that binary

77 mixture of $Fe(OH)_3$ with $Al(OH)_3$ or $SiO_{2(am)}$ have exhibited different adsorption properties from
78 their component parts due to changes in surface site availability and surface charge. This has been
79 ascribed to the dissolution of $Al(OH)_3$ or $SiO_{2(am)}$ and sorption/precipitation of the dissolved ions
80 at Fe-oxides surfaces. Other studies[25] have reported that mixtures of MnO_2 with other oxides like
81 Al_2O_3 or $SiO_{2(am)}$ or TiO_2 inhibited MnO_2 reactivity mainly through heteroaggregation between
82 particles and/or adsorption of metal ions released from the second oxides on the MnO_2 surface.
83 Two recent studies[26,27] even showed that Fe oxides inhibited MnO_2 reactivity through
84 heteroaggregation of positively charged Fe oxides particles with negatively charged MnO_2
85 particles, thereby reducing the number of surface sites of MnO_2. However, little is known on how
86 this reactivity is affected under dynamic, flow-through, conditions that are far more prevalent in
87 environmental and/or engineered systems than the static (batch) modes more commonly employed
88 in laboratory studies. This is particularly relevant because dissolved ions and/or redox by-
89 products (*e.g.* dissolved Mn(II)) concurrently affect surface reactivity of manganese and iron
90 oxides minerals and the mobility of target compounds. As such, experimental work under
91 continuous flow conditions can better emulate natural environments (e.g. geochemical systems
92 containing Fe- and Mn- oxides) or engineered infiltration systems (e.g. managed aquifer recharge
93 (MAR) and water treatment systems), where the target pollutants and the generated reaction
94 products travel through and are then flushed out of the column system. In addition, most traditional
95 environmental models are based on a single phase or simple system, and little is known on the
96 redox reactivity within complex mineral assemblages. Knowledge of the adsorption and redox
97 reactions that take place in the mixed mineral phases or complex environmental systems and under
98 flow-through conditions is consequently needed to explore contaminant transport.

99 This study aims to assess the roles that co-existing iron and manganese oxides play on the
100 fate and transport of contaminants under conditions of water flow. This was achieved by working

with columns packed with sand microparticles (CS) coated by MnO_2 (MCS), goethite (GCS), or mixed goethite-MnO_2 (MGCS). Pipemidic acid (PIP) was, in turn, chosen as a representative redox-active quinolone antibiotic widely used in human and veterinary medicine[28], and commonly found in ng/L to µg/L levels [29–31] in aquatic environments and agricultural settings[32–34]. Investigation of redox transformation of compounds contacted to reactive minerals is also required for an accurate assessment of ecological impacts of quinolone antibiotics. As the redox reaction is strongly depended on pH value and MnO_2/compound ratio, dynamic flow experiments of PIP were performed with two different MnO_2 amounts in the MGCS system and at pH 5.2 and 7.0, which are within the typical pH range for shallow groundwater and soil pore waters[35]. A transport model that accounts for adsorption and oxidation kinetics was used to predict changes in PIP transport in coated sands under flow. This work additionally explains how goethite-MnO_2 interactions affect PIP reactivity, and potentially how these mechanisms affect similar other environmental emerging contaminants.

2. Materials and Methods

2.1 Synthesis of minerals and coated phases

Pure Fontainebleau quartz sand (200-300 µm; ≤ 0.06 m^2/g) was chosen as an inert support, due to its very low reactivity and aqueous solubility under our experimental conditions[36]. The quartz sand was cleaned with HCl, H_2O_2 and ultrapure water to remove any colloidal or amorphous silica particles and organic/inorganic contaminants (see SI for detailed cleaning procedure). Acid birnessite (MnO_2) prepared according to McKenzie[37] was coated on quartz sand (MCS) as in our previous study[17], and summarized in the SI. Likewise, goethite (α-FeOOH) goethite-coated quartz sand (GCS) were synthesized as described in previous studies[18,38–40], and summarized in the SI. The B.E.T. specific surface area of uncoated goethite and birnessite phases was 81 ± 4 and 65 ± 1 $m^2\ g^{-1}$ respectively, and the point of zero charge (PZC) determined at 298 K in 0.01, 0.1 and 1 M

NaCl solutions by the potentiometric titration method, was pH 9.1 for goethite and 2.4 for birnessite. Coating coverage was thereafter evaluated by total Mn and Fe concentrations of acid digested MCS and GCS. Concentrations, measured by Inductively Coupled Plasma-atomic Emission Spectrometry (ICP-AES), revealed 0.60 ± 0.02 (SD) mg Mn per 1 g of MCS and 6.2 mg ± 0.20 (SD) Fe per 1 g of GCS. These coating amounts are within the previously reported range for natural coated subsurface materials[35,41], and they allow stable coated minerals to be achieved.

The possible dissolution of the used quartz sand was, additionally checked in 1 and 10 g/L sand suspensions that were continuously stirred over a range of pH values (4-10) in pure water or 0.01 M NaCl for up to one month. In all cases, the dissolved silicate concentrations were below the detection limit of the molybdenum blue spectrophotometric method (<1 µM) and ICP-AES (<0.2 µM).

Binary mixtures of iron and manganese oxides (MGCS) were prepared by adding different amounts of MnO_2 suspension to GCS. Small aliquots of MnO_2 suspension were pipetted homogenously over the GCS surface, then mixed with a polypropylene spatula, and dried overnight at room temperature. The resulting solid was thereafter washed four times with 10 mM NaCl to remove any uncoated MnO_2, then dried again at room temperature. Two different MGCS were prepared: 1) 0.05 MGCS and 2) 0.1 MGCS, where 0.05 and 0.1 indicate the percentage of MnO_2 in the MGCS system.

The Mn content in the MGCS was determined by dissolving in 30 mM ascorbic acid following the protocol of Charbonnet et al.[42] and analyzed by ICP/AES. The measured amount was 0.29 ± 0.02 (SD) mg of Mn in 1 g of 0.05 MGCS and 0.60 ± 0.02 (SD) mg of Mn in 1 g of 0.1 MGCS. Scanning electron microscopy (SEM) was applied to study the surface morphology of the MGCS matrix. Samples were examined with a JSM JEOL 7100 F microscope with a field emission gun and an OXFORD Genesis energy-dispersive Xray spectrometer at 20 kV at a working distance

of 5−10 mm and magnifications from 15000× to 30000×. SEM images of MGCS showed a mixture of goethite and MnO_2 particles deposited on the sand (Fig.S1). Due to the extremely low Mn amount in the MGCS, X-ray diffraction could not be used for MGCS characterization.

2.2 Batch and column experiments

Three different sets of batch experiments were conducted to determine the 1) pH dependent adsorption of PIP on GCS with or without Mn(II), 2) pH dependent Mn(II) adsorption on GCS with or without PIP, 3) kinetics of PIP removal on 0.05 MGCS at pH 5.2, and 4) kinetic Mn(II) sorption on MCS and MGCS at pH 5.2 under static conditions. Details on the experimental setup are provided in the SI.

Dynamic breakthrough experiments were conducted at room temperature and under water-saturated conditions. Briefly, 15 g of GCS, MCS or MGCS were packed in glass columns with an internal diameter of 1.6 cm and bed length of 4.7 cm. The column was wrapped with aluminum foils to avoid any photo-induced degradation. The bulk density of the packed MGCS was 1.52 ± 0.05 g/cm^3, and the column pore volume (PV or V_p) was 4 ± 0.1 mL. The column was first saturated with a background solution of 10 mM NaCl (previously purged with N_2) at pH 5.2 or 7.0 (depending on the experimental pH) with a constant flow rate of 0.5 mL/min (residence time of 8 min). A bromide tracer experiment was performed using an input solution containing 10 mM NaBr in 10 mM NaCl at pH 5.2 or 7.0. Br^- breakthrough curves for different columns (GCS, MCS, 0.05 MGCS, 0.1 MGCS) were obtained by analysis of the effluent solution using ion chromatography (Fig. S2).

Different column experiments were performed by injecting input solutions consisting of a constant amount of 10 mM NaCl and 10 μM PIP but at two different pH values, 5.2 (± 0.1) or 7.0 (± 0.1). The investigated inflow concentration of PIP may appear higher than the level amounts of pharmaceuticals commonly detected in environmental systems[29-31], but close to total dose of

organic compounds found in industrial effluents or urban stormwater and municipal wastewater used in aquifer recharge[42]. Furthermore, since the Mn-based redox reaction is strongly dependent on red/ox ratio, different MnO_2 amounts and thus different PIP/MnO_2 ratio were investigated. The experimental flow-rate was constant throughout the course of the experiment at 0.5 ml/min. The input solution was purged with N_2 to avoid CO_2 contamination and to maintain the experimental pH throughout the course of the experiment. Flow interruption method was applied in selected experiments to check the occurrence of kinetic limitations. All effluent solutions were collected using a fractional collector. The pH of the effluent solution was determined through the experiment by using an online pH meter. The effluent solution was also analysed for PIP and by-products with high-performance liquid chromatography (HPLC) and an ultrahigh-performance liquid chromatography−tandem mass spectrometry (UPLC-MS/MS) system, and for dissolved metal ions using ICP-AES. More details about experimental conditions and measurements are reported in the SI (Table S1).

2.4 Transport modeling

First, the hydrodynamic parameters were obtained by fitting the bromide breakthrough data using classical Advection Dispersion Equation (ADE):

$$\frac{\partial C}{\partial t} = D\frac{\partial^2 C}{\partial x^2} - v\frac{\partial C}{\partial x} \quad (1)$$

Breakthrough curves (BTC) for Br^- suggest the absence of great dispersion/diffusion or physical nonequilibrium effect (Fig. S2 in the SI). Macroscopic dispersivity (~ 1.89 mm) was obtained by the ratio of the dispersion coefficient (*D*) and of pore velocity (*v*). Molecular diffusion was considered negligible with respect to the dynamic dispersion. The Péclet number (Pe = *v*L/D) was ~25 in the column, suggesting the predominance of a convective regime, and the flow can be assumed to be homogeneous. During water saturation and tracer experiments, total dissolved Mn,

Fe and Si in the outflow was below the ICP-AES detection limit (0.1 μM for Mn, 0.2 μM for Fe and 0.2 μM of Si), and therefore the possibility of mobilization and/or dissolution of minerals can be excluded. Blank tests conducted also confirmed no adsorption of Mn(II) ions to the quartz sand (≤ 0.06 m^2/g).

The reactive transport model is based on a two-site, advective-dispersive transport model with degradation and Freundlich-Langmuir kinetic sorption. The liquid and sorbed concentrations are ruled by the following differential equation that governs the chemical non-equilibrium transport for a homogeneous system under steady-state water flow[43,44]:

$$\frac{\partial C}{\partial t} + \frac{\rho \partial (S)}{\theta \partial t} = D\frac{\partial^2 C}{\partial x^2} - v\frac{\partial C}{\partial x} - \mu_l C - \frac{\rho}{\theta}\mu_s S \quad (2)$$

where θ is the volumetric water content (L^3/L^3), C is the volume-averaged solution concentration (M/L^3), t is time (T), ρ is solid bulk density, S is the sorbed concentration (M/M), D is the dispersion coefficient in the liquid phase (L^2/T), v is the water velocity (L/T), μ_l and μ_s are first-order degradation rate constants (T^{-1}) for the liquid and sorbed phases.

Because quinolones binding to oxide surfaces may proceed through a non-specific and fast surface complexation reaction, such as outer-sphere or hydrogen-bound, and a specific surface complexation reaction, generally slower, such as metal-bound complexes, we assume that adsorption sites can be divided into two fractions, instantaneous (Type-1) and kinetic (Type-2) sites[44].

$$S = S_1 + S_2 \quad (3)$$

Where S_1 and S_2 are solid phase concentrations associated with Type-1 and Type-2 sites respectively. Considering Type-1 adsorption sites are always at equilibrium, S_1 can be expressed as:

$$S_1 = fK\frac{C^\beta}{1+\eta C^\beta} \quad (4)$$

The Type-2 adsorption sites are assumed to be a first-order kinetic rate process:

$$\frac{\partial S_2}{\partial t} = \alpha \left[(1-f) K \frac{C^{\beta}}{1+\eta C^{\beta}} - S_2 \right] - \mu_s S_2 \quad (5)$$

where α is a first-order kinetic rate coefficient (T^{-1}), f is the fraction of instantaneous adsorption sites (Type-1), and K, β and η are empirical coefficients.

Transport modeling was performed with HYDRUS 1D[43]. This code allows for the numerical resolution of equations 2-5 for several boundary and initial conditions: concentration flux at the inlet, zero concentration gradient at the outlet, and no solute at time zero. By using a least-squares optimization routine, HYDRUS 1D also allows inverse modeling to fit the model solution to the data to estimate fate and transport parameters[43]. Because of PIP transformation reactions only occurred at MnO_2 surfaces and not in solution, μ_l was set to 0. This also allows reducing the number of estimated parameters, and thus avoiding non-uniqueness issues (a sensitivity analysis has been done in previous work[7]). Values for the sorption parameter *K*, fraction of equilibrium sites *f*, kinetics adsorption α and the first-order degradation rate μ_s were determined through fitting the breakthrough curves of PIP, and are reported in Table S2.

3. Results and Discussion

3.1. Influence of goethite and/or birnessite coating on the PIP breakthrough

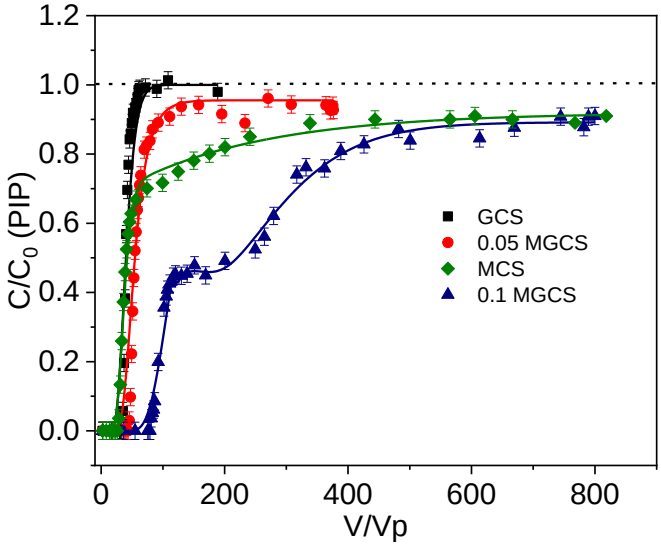

Figure 1. PIP Breakthrough curves MnO_2-bearing columns (0.60 mg Mn/g MCS; 0.29 mg Mn/g 0.05 MGCS; 0.60 mg Mn/g 0.1 MGCS). The dashed line indicates the theoretical complete breakthrough of PIP ($C/C_0 = 1$), and solid lines are model predictions. Inflow conditions: 10 µM PIP; pH 5.2 ± 0.1; 10 mM NaCl; PV 4 mL; flow rate 0.5 mL/min. V/Vp is the ratio of injected volume and pore volume).

MnO_2 in MGCS columns strongly slows down PIP mobility with respect to the (MnO_2-free) GCS column (Figure 1). This can be appreciated by extensive tailing of the breakthrough curve (BTC) and incomplete breakthrough of PIP in the MCS column (0.60 mg Mn/g 0.1 MCS), compared to the GCS column with a sigmoidal-shaped low-tailing BTC with total breakthrough ($C/C_0 = 1$) by 60 PV. In strong contrast, the 0.1 MGCS with the same Mn loading as MCS (0.60 mg Mn/g 0.1 MGCS) exhibited breakthrough at 81 PV, achieved a brief steady-state just below ~200 PV at $C/C_0 \sim 0.45$ and a final steady-state at $C/C_0 \sim 0.91$, just as in MCS, after 744 PV. However, halving Mn loadings to 0.29 mg Mn/g in 0.05 MGCS produced BTC attributes

intermediate to those of GCS and MCS, with the breakthrough point of PIP at 45 PV and a steady breakthrough at $C/C_0 \sim 0.94$ at 308 PV.

The pH of the output solution from the GCS column initially slightly decreased by ~ 0.4 unit but finally returned to 5.5 when steady-state breakthrough was reached (Fig. S3). However, the transformation of PIP on MnO_2 or the reductive conversion of MnO_2 released Mn(II) through:

$$MnO_2 + 2e^- + 4H^+ \rightarrow Mn^{2+} + 2H_2O \quad (6)$$

As this is a proton-promoted process, pH initially increased to 5.9 and then decreased to initial pH value on MCS column (Fig. S3). In the MGCS column, no pH changes in 0.05 MGCS, while pH followed the same behavior as for the MCS column in 0.1 MGCS (Fig. S3). As PIP was mostly present in the zwitterionic form (pKa_1 = 5.20, pKa_2 = 6.38) (Fig. S4), adsorption to goethite occurred via surface complexation reactions involving carboxylic and keto groups, with a possibility of oxidation reaction involving the piperazine ring.[45] However, the BTC shape and the lack of by-products in the effluent did not provide evidence for PIP oxidation by goethite. The modeling results also support the absence of PIP oxidation since no heterogeneous degradation rate (μ_s) was required to fit the BTC of PIP (Fig. 1, Table S2). Conversely, modeling of the partial PIP breakthrough in the Mn-bearing MCS and MGCS columns did require μ_s (Fig. 1, Table S2).

The total amount of PIP removal (by adsorption and/or oxidation) was calculated by integrating of the area above the BTC of PIP. In the MCS column, the total PIP removal was ~5 μmol at ~800 PV, while the same Mn loadings in the 0.1 MGCS column removed ~11 μmol PIP at the same breakthrough time. This consequently implies that the 0.1 MGCS column removed almost twice the amount of PIP than in the MCS column despite having the same Mn loading. As the 0.1 MGCS and GCS columns contained the same goethite loadings, the contribution of goethite in PIP removal can be estimated at ~1.5 μmol.

Enhanced MnO_2 content not only improved PIP removal in the MGCS column (3.2 μmol PIP removal in 0.05 MGCS column vs 11 μmol in 0.1 MGCS column), but also modified the breakthrough behavior. Indeed, a two-step behavior, two fronts and two plateaus, was observed corresponding to the pH variation during the transport experiment (Fig.S3). This breakthrough behavior can be described by considering three stages, and different parameters are necessary to describe each stage of the full BTC of PIP (Table S2). If the same adsorption and oxidation parameters (i.e. α, K, f, μ_s) were used for full BTC description, the calculated curve failed to describe the transport process of PIP, especially for the transitional plateau (Fig. S5). This mobility behavior could be explained by the pH impact on heterogeneous redox reaction and/or (re)adsorption of redox products. It has been reported that fluoroquinolone binding to negatively charged Mn-oxide surfaces proceeds through a heterogeneous redox reaction, whereby two one-electron-transfer or a single two-electron transfer oxidize PIP and reduce surface-bound metal sites [17,19,46]. This will be investigated in the next section.

3.2. Impact of manganese oxide content on PIP oxidation in column

To further investigate PIP transport in MGCS columns, redox by-products (dissolved Mn(II) and oxidized by-product of PIP) were monitored in the outflow solution throughout the breakthrough experiment and upon flow interruption. Our flow/no flow/flow sequence protocol allowed us to check kinetic limitations through determination of BTC of species before interruption and after resumption of flow.

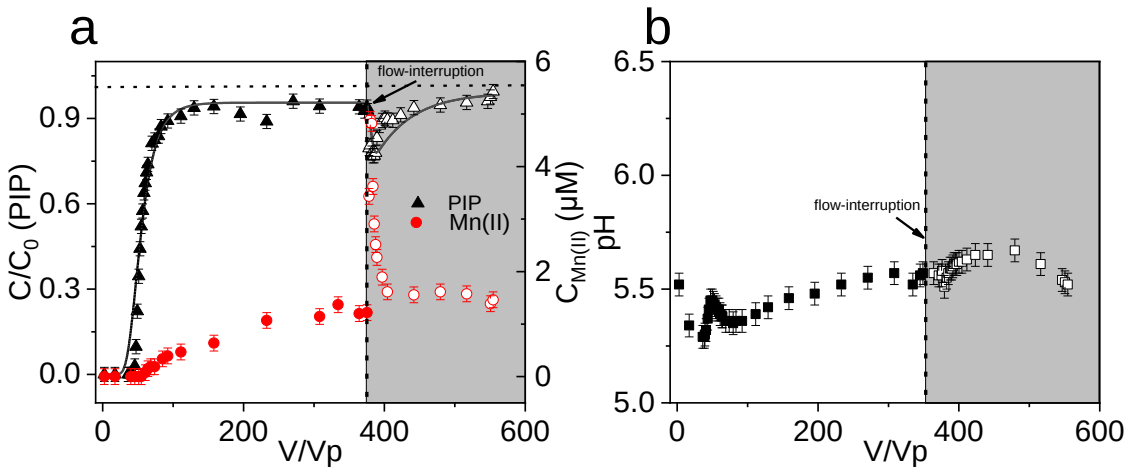

Figure 2. Breakthrough curves of a) PIP, Mn(II), and b) pH in the 0.05 MGCS column. The horizontal dashed line indicates the theoretical complete breakthrough of PIP ($C/C_0 = 1$) and solid lines are model predictions. The vertical dashed lines indicate the moment of flow interruption (duration 24 h). The empty symbols in the shadow area indicate the second-stage after flow resumption. Inflow conditions: 10 μM PIP; pH 5.2 ± 0.1; 10 mM NaCl; PV 4 mL; flow rate 0.5 mL/min. V/Vp is the ratio value of injected volume and pore volume.

In the 0.05 MGCS column, Mn(II) was detected in the effluent solution at the same time as PIP, then reached a steady-state concentration of 1.2 μM. Increasing the residence time of PIP in the 0.05 MGCS column by interrupting the flow for 24 h (376 PV) did not influence the incomplete breakthrough as the same partial breakthrough ($C/C_0 = 0.94$) was still observed upon flow resumption (Fig. 2a). This flow interruption period allowed species to react over a longer period during flow-through conditions. Here, relative concentrations of PIP dropped from 0.94 to 0.76 while those of Mn(II) increased sharply from 1.2 to 5 μM, yet solution pH values were stable throughout the course of the experiment (Fig. 2b). This behavior pointed to rate-limited sorption/redox processes from co-occurring adsorption reactions and heterogeneous redox reactions. Note that BTC curves in separate bromide tracer experiments did not change following

a flow/no-flow/flow sequence, thereby excluding the possibility of physical non-equilibrium or diffusive mass transfer that might cause changes in PIP and Mn(II) concentrations. Upon flow resumption, both PIP and Mn(II) concentrations reached the steady-state concentrations prior to the stop-flow. Although Mn(II) was detected by ICP-AES as the reduced by-product, no oxidized by-product of PIP (hereafter referred as PIP_{ox}) was detected in the effluent throughout the course of the experiment (Fig. 2a). This could be explained by the very low concentrations of generated redox products and/or strong binding to minerals at the working pH value (5.2).

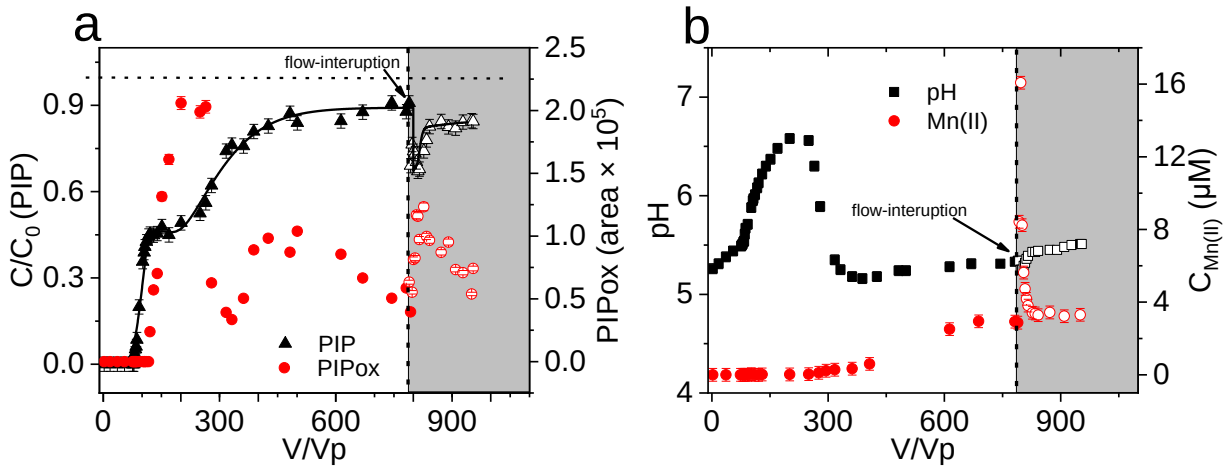

Figure 3. Breakthrough curves of (a) PIP and PIP_{ox} (peak area of PIP by-product; M-26) and (b) Mn(II), pH in 0.1 MGCS column. The horizontal dashed line indicates the theoretical complete breakthrough of PIP (C/C_0 = 1) and solid lines are model predictions. The vertical dashed lines indicate the moment of flow interruption (duration 24 h). The empty symbols in the shadow area indicate the second-stage after flow resumption. Inflow conditions: 10 μM PIP; pH 5.2 ± 0.1; 10 mM NaCl; PV 4 mL; flow rate 0.5 mL/min. V/V_p is the ratio of injected volume and pore volume.

In the 0.1 MGCS column, redox products (Mn(II) and PIP_{ox}) were detected throughout the course of the experiment (Fig. 3a). LC/MS analysis confirmed the PIP_{ox} had a *m*/*z* value of 227 (M-26), formed through N-dealkylation of the piperazine ring of PIP (Fig. S6). As previously

observed for quinolone compounds[17,19], one electron is transferred from sorbed compound to the surface-bound Mn^{IV}, yielding radical intermediates, and Mn^{III} that can be further reduced to give Mn^{II} as follows:

$$\equiv Mn^{IV} + PIP \rightarrow \equiv Mn^{IV} - PIP_{ad} \rightarrow \equiv Mn^{III}/Mn^{II} - PIP^{+} \rightarrow Mn^{II} + PIP_{ox} \quad (7)$$

As seen in Figure 3a, PIP_{ox} concentration in the effluent solution reached its maximum, and then decreased after ~175 PV. Prior to flow-interruption, the BTC of PIP_{ox} followed the outflow pH values, as PIP_{ox} binding to minerals is pH-dependent. However, the peak area of LC/MS data corresponding to PIP_{ox} was not constant (no-steady-state values) during the course of the experiment. Increasing the residence in the column with flow-interruption, decreased PIP concentration but increased that of PIP_{ox}. When the flow was resumed, PIP concentration reached again a plateau, with a steady-state value lower than that before flow interruption (0.9 to 0.8). High MnO_2 content exhibited greater removal ability of PIP and more Mn(II) generation. For example, a higher *k* value, first-order degradation rate coefficient (including sorption and oxidation), was obtained in the 0.1 MGCS (k =2.1×10^{-4} min^{-1}) compared to 0.05 MGCS (k =1.4×10^{-4} min^{-1}), by:

$$k = -\frac{In(\frac{Ca}{C_b})}{t} \quad (8)$$

Here, C is the PIP effluent concentration before (C_b) and after (C_a) flow-interruption, and *t* is the duration of interruption (24 h).

The shape of the breakthrough curve of Mn(II) in the 0.1 MGCS column was similar to that of 0.05 MGCS column. However, Mn(II) did not exhibit breakthrough with PIP (as the 0.05 MGCS column) and was only detected after injection of ~300 PV. This delayed Mn(II) breakthrough corresponds to an increase in the outflow pH value (see Fig. 3b), and thus can be explained by increasing in Mn(II) binding onto goethite with increasing pH (See batch data in Fig. S7). The effluent concentration of Mn(II) thereafter reached a plateau-like, steady-state, value when the pH

decreased down to the inflow pH (~5.2). In MCS no Mn(II) desorbed into the effluent solution (Fig. S8). The presence of dissolved Mn(II) in outflow solutions of MGCS columns (0 μM in MCS column *vs.* 2.5 μM in 0.1 MGCS column at pH 5.2) suggests that the presence of goethite altered Mn(II) uptake by MnO_2 at this pH value, and thus increased its mobility through the column system. This was confirmed further by Mn(II) batch adsorption data on MCS and MGCS (Fig. S9), where 70% of dissolved Mn(II) were removed by MCS while only 40% was removed with MGCS under the same experimental conditions (See Fig. S9). Additional batch experiments showed that PIP was continuously removed (sorption + oxidation) by MGCS, yet only Mn(II) (no PIP_{ox}) was detected in solution (Fig. S10). As observed in the column system, the presence of goethite likely ensured preferential adsorption of PIP or PIP_{ox} over Mn(II) onto MGCS at pH 5.2. This aligns with our batch adsorption tests (Fig. S7) revealing strong PIP and weak Mn(II) loadings at this pH value. PIP binding was also lower and Mn(II) binding greater at larger pH, and even because competitive sorption at pH > 6. Taken together, these findings confirmed that interactions between positively charged goethite (PZC 9.1) and negatively charge MnO_2 (PZC 2.4) particles decreased overall cation adsorption in the MGCS system. As a result, dissolved Mn(II) ion was flushed out of the column, thus preventing further interactions with MnO_2 and mitigating surface passivation, which is generally observed in MnO_2–based redox reactions (*e.g.* as in MCS column) [4,17,42]. Indeed, it has been reported that Mn(II) binding at the MnO_2 surface may decrease the oxidation rate of organic compounds because (i) Mn(II) may block redox reactive sites on the oxide surface, preventing adsorption of the organic compound or competitively reacting with MnO_2 and (ii) surface bound Mn(II) may decrease the average oxidation state of MnO_2, and therefore slow the rate of electron transfer [4,17,42,46]. This may explain the higher reactivity of the MGCS system in total PIP removal with respect to MCS.

3.3. PIP transport at two pH values

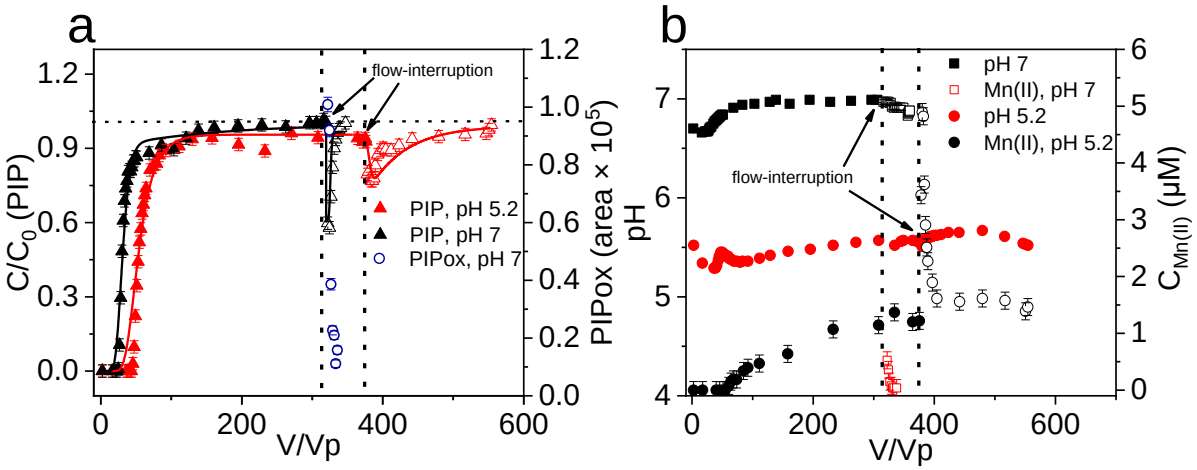

Figure 4. Breakthrough curves of (a) PIP and PIP_{ox} (peak area of PIP by-product; M-26) and (b) Mn(II), pH on different pHs in 0.05 MGCS column. The horizontal dashed line indicates the theoretical complete breakthrough of PIP (C/C_0 = 1) and solid lines are model predictions. The vertical dashed lines indicate the moment of flow interruption (duration 24 h). The empty symbols indicate the second-stage after flow resumption. Inflow conditions: 10 μM PIP, pH 5.2 ± 0.1 and 7.0 ± 0.1, 10 mM NaCl, PV 4 mL, flow rate 0.5 mL/min. V/Vp is the ratio of injected volume and pore volume.

An additional PIP breakthrough experiment in 0.05 MGCS column was repeated but at pH 7.0. In contrast to experiments at pH 5.2 (Fig. 4), no variations in pH occurred. Only 1.8 μmol of PIP was removed at neutral pH, compared to that at pH 5.2 (3.2 μmol), because acidic conditions favored PIP oxidation and adsorption onto MnO_2 and/or goethite. Steeper BTC and earlier breakthrough point, with complete breakthrough were achieved, whereas no PIP_{ox} or Mn(II) was detected in the column effluent, indicating extreme low or no PIP transformation occurred at pH 7. This observation is consistent with our modeling result since setting $\mu_s = 0$ can well fit the BTC of PIP at pH 7 (Table S2).

No oxidation occurred during the first stage, but when the residence time is increased, Mn(II) and PIP_{ox} were detected upon flow resumption. The PIP relative concentration drops to 0.6 at pH 7 but only to 0.8 at pH 5.2 when the flow was resumed (Fig. 4a). According to Eq. 8, more PIP was removed and a higher *k* value was obtained during flow interruption period at pH 7 (1.4×10^{-4} min^{-1} at pH 5.2, 3.5×10^{-4} min^{-1} at pH 7, Table S3). As only sorption happened in the first step, we suppose that the pristine MnO_2 surfaces may enable more PIP oxidation during flow interruption period. Furthermore, less MnO_2 passivation can be expected, as more Mn(II) can be adsorbed by goethite at pH 7 (see batch data in Fig. S7).

In summary, both experimental and modeling results show that binary mixtures of manganese oxides and goethite are capable of oxidizing and removing PIP more efficiently than in the single phase. MGCS may overcome the major drawbacks of MCS to be used as a potential geomedia for antibiotic removal. Indeed, preferential adsorption of Mn(II) on negatively charged MnO_2, and the progressive build-up of Mn(II) in the column decreased the reactivity of the MCS column over breakthrough time. However, MGCS preferential adsorbed PIP or PIP_{ox} over Mn(II) and thereby reduced the passivation effect by dissolved Mn(II).

4. Environmental significance

This study contributed to mounting evidences that the environmental fate of pollutants can not be predicted based on the sorption/oxidation data of single minerals. A thorough examination of the redox reactivity within complex mineral assemblages under both batch and continuous flow conditions is necessary for an accurate assessment of contaminant transport in natural environments (e.g. soils and sediments) or engineered infiltration systems (e.g. MAR). Here, we showed that coexisting minerals, in our case goethite, can alter the overall reactivity of the redox-active MnO_2. In particular, interactions between the positively charged goethite and the negatively charged MnO_2

particles decreased Mn(II) surface loadings, thus facilitating its mobility through the column. In addition to advancing ideas on environmental processes, knowledge that goethite-MnO_2 interactions decrease MnO_2 passivation could be used to design novel geomedia filters. Fe and Mn binary oxide may overcome the major drawbacks of Mn-oxides to be used as a potential geomedia for antibiotic removal. As manganese oxides have the potential to be applied as filter to prevent organic contaminants from percolating into the groundwater sources in both natural soils and artificial infiltration systems, this work could help in designing efficient geomedia in treatment technologies (industrial and/or municipal wastewater, agricultural runoff, stormwater, etc.). Those contaminated systems contain diverse organic groups such as pharmaceuticals and personal care products, pesticides and detergents, with varying concentrations. Therefore, the amount MnO_2 and/or goethite coated on sand should be optimized to further enhance the reactivity and longevity of geomedia, and prior to the application of GMCS in infiltration systems. Finally, as Fe and Mn-oxides may co-exist with each other as particulate coatings, the transport model developed here will help in understanding fate and transformation of emerging compounds in natural environments such as soils and sediments.

Supporting Information

Synthesis of minerals and coatings materials; pH dependent PIP and Mn(II) adsorption onto GCS; Kinetics of PIP removal with 0.05 GMCS; Kinetic sorption of Mn(II) on MCS and 0.05 GMCS; PIP and PIP_{ox} detection methods; SEM images of GCS, 0.05 MGCS, 0.1 MGCS; Breakthrough curves of pH in the different MnO_2 content packed columns.

Author Contributions

† T.L. and R.P. contributed equally to this work.

Notes

444 The authors declare no competing financial interest.

445 **Acknowledgements**

446 The authors acknowledge the support of the Institut Universitaire de France, the Swedish Research
447 Council (2020-04853), the French National Research Agency via the INFLOW project (ANR-21-
448 CE29-0008-01) and the CNRS (IEA 2018-2020). We also thank the China Scholarship Council for
449 a Ph.D. grant and Région Bretagne for a mobility grant for an extended research stay at Umeå
450 University.

451

References

(1) Post, J. E. Manganese Oxide Minerals: Crystal Structures and Economic and Environmental Significance. *Proc. Natl. Acad. Sci. U. S. A.* **1999**, *96* (7), 3447–3454.

(2) Cornell, R. M.; Schwertmann, U. *The Iron Oxides: Structure, Properties, Reactions, Occurrences and Uses*; Weinheim: Wiley-vch, 2003.

(3) Lion, L. W.; Altmann, R. S.; Leckie, J. O. Trace-Metal Adsorption Characteristics of Estuarine Particulate Matter: Evaluation of Contributions of Fe/Mn Oxide and Organic Surface Coatings. *Environ. Sci. Technol.* **1982**, *16* (10), 660–666.

(4) Remucal, C. K.; Ginder-Vogel, M. A Critical Review of the Reactivity of Manganese Oxides with Organic Contaminants. *Environ. Sci. Process. Impacts* **2014**, *16* (6), 1247–1266.

(5) Li, J.; Zhao, L.; Zhang, R.; Teng, H. H.; Padhye, L. P.; Sun, P. Transformation of Tetracycline Antibiotics with Goethite: Mechanism, Kinetic Modeling and Toxicity Evaluation. *Water Res.* **2021**, *199*, 117196.

(6) Huang, X.; Chen, Y.; Walter, E.; Zong, M.; Wang, Y.; Zhang, X.; Qafoku, O.; Wang, Z.; Rosso, K. M. Facet-Specific Photocatalytic Degradation of Organics by Heterogeneous Fenton Chemistry on Hematite Nanoparticles. *Environ. Sci. Technol.* **2019**, *53* (17), 10197–10207.

(7) Zhou, L.; Martin, S.; Cheng, W.; Lassabatere, L.; Boily, J. F.; Hanna, K. Water Flow Variability Affects Adsorption and Oxidation of Ciprofloxacin onto Hematite. *Environ. Sci. Technol.* **2019**, *53* (17), 10102–10109.

(8) Chen, Y.; Lu, X.; Liu, L.; Wan, D.; Chen, H.; Zhou, D.; Sharma, V. K. Oxidation of B-Blockers by Birnessite: Kinetics, Mechanism and Effect of Metal Ions. *Chemosphere* **2018**, *194*, 588–594.

(9) Liang, M.; Xu, S.; Zhu, Y.; Chen, X.; Deng, Z.; Yan, L.; He, H. Preparation and Characterization of Fe-Mn Binary Oxide/Mulberry Stem Biochar Composite Adsorbent and Adsorption of Cr(VI) from Aqueous Solution. *Int. J. Environ. Res. Public Health* **2020**, *17*, 676.

(10) Ricko, A. N.; Psoras, A. W.; Sivey, J. D. Reductive Transformations of Dichloroacetamide Safeners: Effects of Agrochemical Co-Formulants and Iron Oxide + Manganese Oxide Binary-Mineral Systems. *Environ. Sci. Process. Impacts* **2020**, *22* (10), 2104–2116.

(11) Zhang, G.; Liu, F.; Liu, H.; Qu, J.; Liu, R. Respective Role of Fe and Mn Oxide Contents for Arsenic Sorption in Iron and Manganese Binary Oxide: An X-Ray Absorption Spectroscopy Investigation. *Environ. Sci. Technol.* **2014**, *48* (17), 10316–10322.

(12) Liu, H.; Chen, T.; Frost, R. L. An Overview of the Role of Goethite Surfaces in the Environment. *Chemosphere* **2014**, *103*, 1–11.

(13) Evanko, C. R.; Dzombak, D. A. Surface Complexation Modeling of Organic Acid Sorption to Goethite. *J. Colloid Interface Sci.* **1999**, *206*, 189–206.

(14) Cheng, W.; Zhou, L.; Marsac, R.; Boily, J. F.; Hanna, K. Effects of Organic Matter–Goethite Interactions on Reactive Transport of Nalidixic Acid: Column Study and Modeling. *Environ. Res.* **2020**, *191*, 110187.

(15) Wang, L.; Cheng, H. Birnessite (γ-MnO2) Mediated Degradation of Organoarsenic Feed Additive p -Arsanilic Acid. *Environ. Sci. Technol.* **2015**, *49* (6), 3473–3481.

(16) Zhao, W.; Tan, W.; Wang, M.; Xiong, J.; Liu, F.; Weng, L.; Koopal, L. K. CD-MUSIC-EDL Modeling of Pb^{2+} Adsorption on Birnessites: Role of Vacant and Edge Sites. *Environ. Sci. Technol.* **2018**, *52* (18), 10522–10531.

(17) Pokharel, R.; Li, Q.; Zhou, L.; Hanna, K. Water Flow and Dissolved Mn(II) Alter Transformation of Pipemidic Acid by Manganese Oxide. *Environ. Sci. Technol.* **2020**, *54* (13), 8051–8060.

(18) Hanna, K.; Boily, J. F. Sorption of Two Naphthoic Acids to Goethite Surface under Flow through Conditions. *Environ. Sci. Technol.* **2010**, *44* (23), 8863–8869.

(19) Zhang, H.; Huang, C. H. Oxidative Transformation of Fluoroquinolone Antibacterial Agents and Structurally Related Amines by Manganese Oxide. *Environ. Sci. Technol.* **2005**, *39* (12), 4474–4483.

(20) Wang, A.; Wang, H.; Deng, H.; Wang, S.; Shi, W.; Yi, Z.; Qiu, R.; Yan, K. Controllable Synthesis of Mesoporous Manganese Oxide Microsphere Efficient for Photo-Fenton-like Removal of Fluoroquinolone Antibiotics. *Appl. Catal. B Environ.* **2019**, *248* (July 2018), 298–308.

(21) Cheng, W.; Elaheh, Lot, K.; Remi, M.; Hanna, K. Adsorption of Quinolone Antibiotics to Goethite under Seawater Conditions: Application of a Surface Complexation Model. *Environ. Sci. Technol.* **2019**, *53*, 1130–1138.

(22) Anderson, P. R.; Benjamin, M. M. Surface and Bulk Characteristics of Binary Oxide Suspensions. *Environ. Sci. Technol.* **1990**, *24* (5), 692–698.

(23) Anderson, P. R.; Benjamin, M. M. Modeling Adsorption in Aluminum-Iron Binary Oxide Suspensions. *Environ. Sci. Technol.* **1990**, *24* (10), 1586–1592.

(24) Meng, X.; Letterman, R. D. Effect of Component Oxide Interaction on the Adsorption Properties of Mixed Oxides. *Environ. Sci. Technol.* **1993**, *27* (5), 970–975.

(25) Taujale, S.; Zhang, H. Impact of Interactions between Metal Oxides to Oxidative Reactivity of Manganese Dioxide. *Environ. Sci. Technol.* **2012**, *46*, 2764–2771.

(26) Zhang, H.; Taujale, S.; Huang, J.; Lee, G. Effects of NOM on Oxidative Reactivity of Manganese Dioxide in Binary Oxide Mixtures with Goethite or Hematite. *Langmuir* **2015**, *31*, 2790–2799.

(27) Huang, J.; Zhang, H. Redox Reactions of Iron and Manganese Oxides in Complex Systems. *Front. Environ. Sci. Eng.* **2020**, *14* (5), 76.

(28) Shimizu, M.; Nakamura, S.; Kurobe, N.; Takase, Y. Absorption, Distribution and Excretion of Pipemidic Acid. *Chemotherapy* **1975**, *23* (9), 2724–2729.

(29) Golet, E. M.; Alder, A. C.; Giger, W. Environmental Exposure and Risk Assessment of Fluoroquinolone Antibacterial Agents in Wastewater and River Water of the Glatt Valley Watershed, Switzerland. *Environ. Sci. Technol.* **2002**, *36* (17), 3645–3651.

(30) Kolpin, D. W.; Furlong, E. T.; Meyer, M. T.; Thurman, E. M.; Zaugg, S. D.; Barber, L. B.; Buxton, H. T. Pharmaceuticals, Hormones, and Other Organic Wastewater Contaminants in U.S. Streams, 1999-2000: A National Reconnaissance. *Environ. Sci. Technol.* **2002**, *36* (18), 1202–1211.

(31) Hartmann, A.; Golet, E. M.; Gartiser, S.; Alder, A. C.; Koller, T.; Widmer, R. M. Primary DNA Damage but Not Mutagenicity Correlates with Ciprofloxacin Concentrations in German Hospital Wastewaters. *Arch. Environ. Contam. Toxicol.* **1999**, *36* (2), 115–119.

(32) Weist, K.; Högberg, L. D. ECDC Publishes 2015 Surveillance Data on Antimicrobial Resistance and Antimicrobial Consumption in Europe. *Eurosurveillance* **2016**, *21*, 30401.

(33) Ma, Y.; Li, M.; Wu, M.; Li, Z.; Liu, X. Occurrences and Regional Distributions of 20 Antibiotics in Water Bodies during Groundwater Recharge. *Sci. Total Environ.* **2015**, *518–519*, 498–506.

(34) Manyi-Loh, C.; Mamphweli, S.; Meyer, E.; Okoh, A. Antibiotic Use in Agriculture and Its Consequential Resistance in Environmental Sources: Potential Public Health Implications. *Molecules* **2018**, *23*, 795.

(35) Sposito, G. *The Surface Chemistry of Soils*; Oxford university press. 1984.

(36) Zhou, L.; Cheng, W.; Marsac, R.; Boily, J. F.; Hanna, K. Silicate Surface Coverage Controls Quinolone Transport in Saturated Porous Media. *J. Colloid Interface Sci.* **2022**, *607*, 347–356.

(37) McKenzie, R. M. The Synthesis of Birnessite, Cryptomelane, and Some Other Oxides and Hydroxides of Manganese. *Miner. Mag.* **1971**, *38*, 493–502.

(38) Gaboriaud, F.; Ehrhardt, J. J. Effects of Different Crystal Faces on the Surface Charge of Colloidal Goethite (α-FeOOH) Particles: An Experimental and Modeling Study. *Geochim. Cosmochim. Acta* **2003**, *67* (5), 967–983.

(39) Hanna, K.; Martin, S.; Quilès, F.; Boily, J.-F. Sorption of Phthalic Acid at Goethite Surfaces under Flow-Through Conditions. *Langmuir* **2014**, *30* (23), 6800–6807.

(40) Rusch, B.; Hanna, K.; Humbert, B. Coating of Quartz Silica with Iron Oxides: Characterization and Surface Reactivity of Iron Coating Phases. *Colloids Surfaces A Physicochem. Eng. Asp.* **2010**, *353* (2–3), 172–180.

(41) Stumm, W. *Chemistry of the Solid–Water Interface: Processes at the Mineral–Water and Particle–Water Interface in Natural Systems*; John Wiley & Son Inc., 1992.

(42) Charbonnet, J. A.; Duan, Y.; Van Genuchten, C. M.; Sedlak, D. L. Chemical Regeneration of Manganese Oxide-Coated Sand for Oxidation of Organic Stormwater Contaminants. *Environ. Sci. Technol.* **2018**, *52* (18), 10728–10736.

(43) Šimůnek, J.; van Genuchten, M. T. Modeling Nonequilibrium Flow and Transport Processes Using HYDRUS. *Vadose Zo. J.* **2008**, *7* (2), 782–797.

(44) Van Genuchten, M. T.; Wagenet, R. J. Two-Site/Two-Region Models for Pesticide Transport and Degradation: Theoretical Development and Analytical Solutions. *Soil Sci. Soc. Am. J.* **1989**, *53* (5), 1303–1310.

(45) Zhang, H.; Huang, C. H. Adsorption and Oxidation of Fluoroquinolone Antibacterial Agents and Structurally Related Amines with Goethite. *Chemosphere* **2007**, *66* (8), 1502–1512.

(46) Li, Q.; Pokharel, R.; Zhou, L.; Pasturel, M.; Hanna, K. Coupled Effects of Mn(II), pH and Anionic Ligands on the Reactivity of Nanostructured Birnessite. *Environ. Sci. Nano* **2020**, *7* (12), 4022–4031.